ACS Photonics
Article
pubs.acs.org/journal/apchd5

Second-Harmonic Generation in GaAs Photonic Crystal Cavities in (111)B and (001) Crystal Orientations

Sonia Buckley,*[†] Marina Radulaski,[†] Jan Petykiewicz,[†] Konstantinos G. Lagoudakis,[†] Ju-Hyung Kang,[‡] Mark Brongersma,[‡,§] Klaus Biermann,[§] and Jelena Vučković[†]

[†]Spilker Center for Engineering and Applied Sciences, Stanford University, Stanford, California 94305, United States
[‡]Department of Materials Science and Engineering, Stanford University, Stanford, California 94305, United States
[§]Paul-Drude-Institut für Festkörperelektronik, Hausvogteiplatz 5-7, D-10117, Berlin, Germany

S *Supporting Information*

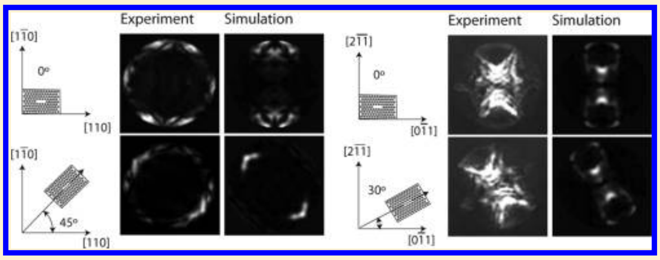

ABSTRACT: We demonstrate second-harmonic generation in photonic crystal cavities in (001)- and (111)B-oriented GaAs. The fundamental resonance is at 1800 nm, leading to generated second harmonic below the GaAs band gap. Below-band-gap operation minimizes absorption of the second-harmonic and two-photon absorption of the pump. Photonic crystal cavities were fabricated in both orientations at various in-plane rotations of the GaAs substrate. The rotation dependence and far-field patterns of the second harmonic match simulation. We observe similar maximum efficiencies of 1.2%/W in (001)- and (111)B-oriented GaAs.

KEYWORDS: *nanophotonics, semiconductor microcavities, photonic crystals, nonlinear optics*

Photonic crystal cavities are excellent candidates for nonlinear optical devices, due to their low mode volume and high quality (Q) factor. As discussed previously,[1,2] in such optical cavities, the optical mode volume is small compared to the material nonlinear coherence length, and the phase matching condition is replaced by the requirement of large mode overlap between the relevant optical modes. This offers an additional advantage for III–V semiconductor materials, which possess high nonlinearity but no birefringence. Many different approaches have been taken in order to overcome this limitation and take advantage of III–V materials, including growth of multiple quantum wells to induce birefringence,[3] orientation patterning for quasi-phase-matching,[4] inversion phase-matching in microdisks,[5] form birefringence in waveguides,[6] surface emitting cavities,[7] and integration with optical microcavities.[8] Integration of III–V materials with photonic crystal cavities requires only standard semiconductor processing,[9] while the geometry of these cavities also allows easy integration of active gain media such as quantum dots or quantum wells,[10−12] as well as potential on-chip integration with detectors, switches, and modulators.

Experimentally, there have been many recent demonstrations of high efficiency, low-power $\chi^{(2)}$ nonlinear processes in resonant microcavities, in particular second-harmonic generation in microdisks[5,13] and microrings[14,15] in materials such as GaAs, GaN, and AlN, as well as second-harmonic generation and sum frequency generation in photonic crystal cavities in materials such as InP,[16] GaP,[17] GaAs,[8,10,12] and $LiNbO_3$.[18] Millimeter-sized lithium niobate microdisks have also been used for high-efficiency second-harmonic generation (SHG) and ultralow threshold optical parametric oscillators (OPOs).[19−21]

In order to achieve efficient nonlinear frequency conversion, it is necessary to choose a material with a nonlinear susceptibility tensor symmetry that matches the symmetry of the cavity modes well[7,8] (e.g., by choosing crystal orientation). For photonic crystal cavities, modes can be described as having either TE-like or TM-like polarization.[22] In the (001) orientation, the only allowed polarization conversion is from TE-like to TM-like modes (or from TM-like to TE-like). Moving to a different crystal orientation, such as the (111) orientation, is equivalent to rotating the electronic crystal axes relative to the photonic crystal axes, and therefore conversions from TE-like to TE-like and TM-like to TM-like modes are also allowed. Additionally, it is important to choose a transparency window that overlaps well with the experimental frequencies. GaAs has a transparency window from around 900 nm to 16 μm and so is particularly useful for nonlinear frequency conversion if all three wavelengths are within this range. Within this frequency range, GaAs is preferable to wider band gap semiconductors such as GaP, as it has a stronger nonlinearity,[23] is easier to grow in the (111) crystal orientation, and is compatible with bright gain media such as InGaAs quantum wells and efficient quantum emitters, such as InAs quantum dots.[10,12,24]

Here, we fabricate perturbed three-hole-defect (L3) photonic crystal cavities in (001)- and (111)B-oriented GaAs. The

Received: February 15, 2014

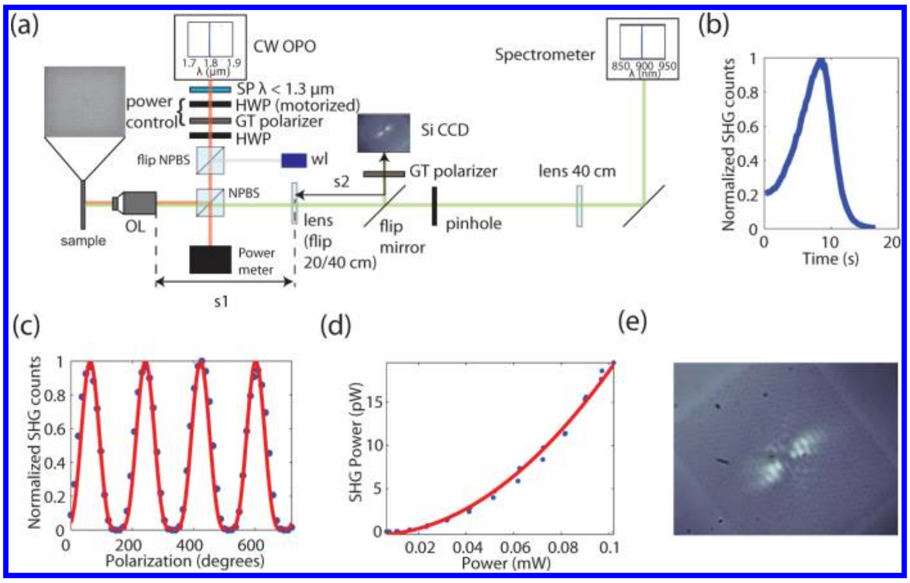

Figure 1. (a) Setup for generation of second harmonic and measurement of the *k*-space. (NP)BS = (nonpolarizing) beamsplitter, HWP = half wave plate, GT = Glan-Thompson, SP = short pass filter, WL = white light source, OL = objective lens. (b) Scanning the temperature of a photonic crystal structure in (111)B-oriented GaAs between 40 and 10 K with the laser wavelength fixed at 1785 nm. SHG signal was measured every 0.2 s (temperature change was not necessarily linear in time) and plotted versus time. This demonstrates the presence of a resonance in this wavelength range, although we cannot extract the *Q*. (c) Scanning the input polarization to the cavity for the same cavity and wavelength as in part (b). (d) SHG power collected through the lens versus input power transmitted through the lens for a structure in (001)-oriented GaAs, with the three hole defect at 60° relative to the [110] or [10] direction with the resonant wavelength at 1799 nm. (e) Real space white light image of a photonic crystal structure in (001)-oriented GaAs with the three-hole defect at 45° to the [110] or $[1\bar{1}0]$ axis with second-harmonic emission also visible on Si CCD (10 mW pump power at 1750 nm). The structure is about 25 × 20 μm.

fundamental mode is at around 1800 nm, and thus the generated second harmonic is below the band gap of the GaAs, leading to minimal absorption[25] and two-photon absorption, which was present in the previous studies in this material[8,12] due to their operation above the band gap. The lack of absorption and other nonlinear absorption effects allows us to more easily simulate the second-harmonic mode and to compare the simulations quantitatively with the experimentally measured far-field momentum space (*k*-space) of the second-harmonic emission. While *k*-space measurements were performed in previous studies[16,17] in other materials, here we expand upon the measurement and simulations of the generated modes, matching the simulated and experimental results, and demonstrate that the modes vary significantly with the photonic crystal cavity parameters and effective nonlinear susceptibility tensor symmetry (i.e., GaAs crystal orientation). Therefore, the semiconductor crystal orientation can be employed in addition to optical cavity design to improve the efficiency of frequency conversion.[8]

LINEAR AND NONLINEAR CHARACTERIZATION OF STRUCTURES

Perturbed L3 photonic crystal cavities, as described in refs 26 and 27, were fabricated in 165 nm thick (001) and (111)B = ($\bar{1}\bar{1}\bar{1}$) oriented GaAs membranes grown on an AlGaAs sacrificial layer (0.878 μm thick in the (001) sample, 0.8 μm thick in the (111)B sample) on n-type doped substrates. The cavities were fabricated using e-beam lithography and dry etching to define the pattern, followed by HF wet etching to remove the sacrificial layer as described previously.[9] The fabricated structures had a lattice constant a = 560−620 nm (resonant wavelengths between 1730 and 1900 nm) and designed hole radius $r_1/a = 0.3$, with perturbed hole radius $r_2/a = 0.33$. We choose these parameters in order to obtain structures with the second harmonic below the band gap of GaAs, but detectable on a Si CCD. Fabricated photonic crystal cavities were all characterized experimentally at the fundamental (first harmonic) wavelength with a broadband LED light source using a cross-polarized reflectivity method,[28] with *Q* factors of 3000 to 4000 measured, with a simulated mode volume of $V = 0.76\ (\lambda/n^3)$.

The setup for characterizing a generated second harmonic is shown in Figure 1a, with the flip mirror down and the 40 cm lens in place for a confocal measurement. Light from a continuous wave optical parametric oscillator was tuned to the resonant wavelength (measured previously via cross-polarized reflectivity) of a particular cavity and was reflected from a beam splitter and coupled to the cavity at normal incidence through a high numerical aperture (NA) objective lens. The laser power was monitored in real time via the transmission port of the beam splitter, and the system was calibrated to calculate the power transmitted through the objective. The laser power incident on the structure was controlled with a half-wave plate (HWP) on a motorized rotation stage, followed by a Glan-Thompson polarizer. The input polarization on the cavity was then controlled by a second HWP after the polarizer. The second harmonic was collected through the same objective lens and transmitted through the beam splitter, where it was collected on a CCD spectrometer. The losses through the objective lens, beam splitter, and other optics were measured, and the spectrometer was calibrated at the wavelength of the second harmonic to obtain the second-harmonic power emitted into the numerical aperture of the objective lens. To verify the SHG is a cavity effect, rather than a bulk GaAs effect, we scanned the resonant wavelength of the cavity across the laser wavelength by scanning the temperature of the sample. While the OPO could be set to the wavelength of our choice, the

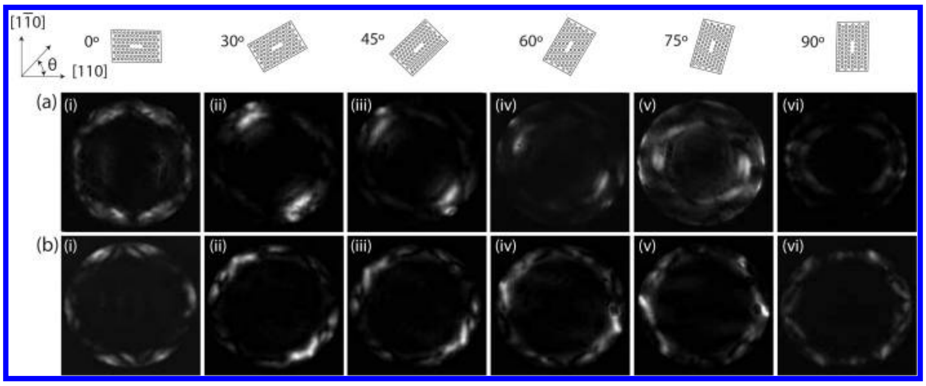

Figure 2. Experimental *k*-space profiles of second-harmonic emission in (001)-oriented GaAs L3 cavities with lattice constants (a) 560 nm (mean fundamental resonance = 1757.5 nm) and (b) 580 nm (mean λ_1 = 1800.3 nm) for in-plane rotations of (i) 0°, (ii) 30°, (iii) 45°, (iv) 60°, (v) 75°, and (vi) 90°.

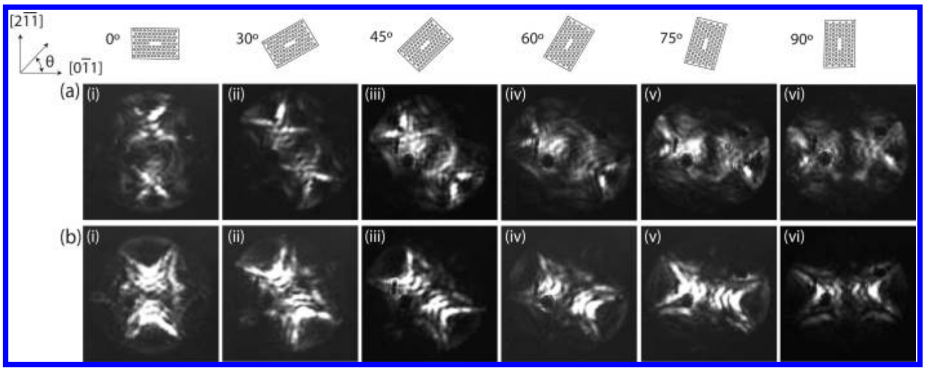

Figure 3. Experimental *k*-space profiles of second-harmonic emission in (111)B-oriented GaAs L3 cavities with lattice constants (a) 600 nm (mean fundamental resonance λ_1 = 1769 nm) and (b) 620 nm (mean λ_1 = 1811 nm) for in-plane rotations of (i) 0°, (ii) 30°, (iii) 45°, (iv) 60°, (v) 75°, and (vi) 90°.

tuning was not smooth, and therefore to obtain a scan over the resonance, it was more convenient to vary the resonant wavelength with temperature, then to scan the laser. For this measurement, the sample was mounted in a liquid helium cryostat, and a Zeiss objective with an NA of 0.75 was used to couple light to the structure. The set temperature of the cryostat was reduced from 40 K to 10 K (this range was found to be sufficient to scan across the resonance while the cryostat remained most stable in this range). As the temperature dropped slowly, the second-harmonic power was measured at equal time intervals. A resulting peak is shown in Figure 1b. We measured the actual temperature only at the start and end points, while the rate of change of temperature versus time as well as the change in resonant wavelength versus temperature would be necessary in order to perform an accurate fit; our previous experiments[17] show that the *Q* factor follows a Lorentzian squared with the same *Q* factor measured in the reflectivity measurement, which in this case was 4000. However, the measurement indicates that the second-harmonic process is sensitive to the resonant wavelength of the cavity.

For subsequent measurements no cryostat was present and an Olympus objective lens with NA 0.95 was used. The OPO was set to the measured wavelength of the cavity. The polarization incident on the cavity was also scanned by varying the HWP angle, as shown in Figure 1c. The SHG intensity follows a $\cos^4 \theta$ dependence on HWP angle θ as shown by the red line fit, as expected from the L3 cavity, which is strongly polarized in the *y*-direction (perpendicular to the line defined by the three-hole defect of the cavity). There is a phase offset as the *x*-axis of the cavity was not aligned to 0° for the polarizer. The second-harmonic power dependence on input power can be recorded by varying the laser power at a particular wavelength with the HWP/polarizer combination; the resulting curve for a typical cavity is shown in Figure 1d, with a quadratic fit in red.

FAR-FIELD MEASUREMENTS

To obtain information about the second-harmonic modes, we imaged the *k*-space of the second-harmonic signal in (001)- and (111)B-oriented wafers for in-plane cavity rotations of 0°, 30°, 45°, 60°, 75°, and 90° relative to the [110] or [1$\bar{1}$0] direction (information about which was not available) of the (001)-oriented wafer and the [1$\bar{1}$0] direction of the (111)-oriented wafer. The setup was in 2*f*–2*f* configuration, as shown in Figure 1a, with the flip mirror up and the 20 cm lens in place such that $s_1 = s_2 = 2f$ = 40 cm. The position of the camera was optimized such that a sharp image of the back aperture of the objective lens was generated. By flipping up the 40 cm lens, we could also image the real-space signal on the camera as shown in Figure 1e.

The measured far-field patterns for lattice constant 560 nm (mean pump wavelength λ_1 = 1757.5 nm, standard deviation 6.5 nm) and 580 nm (mean λ_1 = 1800.3 nm, standard deviation 6.2 nm) in (001)-oriented GaAs are shown in Figure 2, parts a and b, with rotations from 0° to 90° shown. Differences in intensity are unrelated to the actual efficiency of the device; input power was adjusted to keep the images below saturation of the camera, in order to help with identification of the modes (see Supporting Information). The *k*-space images for 0° and 45° in-plane rotations have very different spatial patterns, which we expect since the overlap of the fundamental and second-harmonic mode changes with the rotation of the photonic crystal axes relative to the crystal axes. However, this effect is complicated by slight changes in other parameters. These additional changes for different rotations are due to differences in fabrication at different angles relative to the crystal axes and relative to the e-beam stage, which may cause variations in hole shape with in-plane rotation angle. We observe that the resonant wavelength within a particular rotation in the (001) orientation varies by 3 nm, while the mean resonant wavelength decreases by 17 nm between 0° and 75° rotations (with a slight increase again for 90°). Simulations indicate that the membrane thickness and wavelength have a large effect on the mode observed (see Simulations section). This is consistent with what we observe, as even the 3.5% change in lattice constant from 560 nm to 580 nm with corresponding shift in resonant wavelength from 1760 nm to 1800 nm has a noticeable effect on the far-field, as can be seen in the difference between Figure 2a and b. Additionally, at these wavelengths there is rapidly increasing absorption as the second harmonic approaches the band gap,[25] which could also affect the mode, in particular for the 560 nm lattice constant.

Figure 3 shows the same measurement for the (111)B orientation, with (a) $a = 600$ nm (mean $\lambda_1 = 1769$ nm, standard deviation = 3 nm) and (b) $a = 620$ nm (mean $\lambda_1 = 1811.1$ nm, standard deviation = 3.8 nm). Despite the fact that the membranes were nominally the same thickness, in order to maintain the same resonant wavelength as in the (001) orientation, it was necessary to increase the lattice constant by 40 nm, which indicates either a thinner membrane, larger etched hole radius, or larger refractive index; the exact cause was difficult to determine via SEM images of the structures. In this case, there is again a decrease in average resonant wavelengths across rotations from 0° to 75°, but in this case of only 7.5 nm, while the maximum variation within a rotation is larger (6 nm, although on average it is lower than this). The larger intrarotation variation in the (111)B orientation is likely due to a higher number of surface defects in this wafer.

The mode *k*-space distribution observed is very different for the two orientations and also changes less with rotation of the L3 in the plane of the wafer in the (111)B orientation, which matches our simulations (see Simulations section).

■ SECOND-HARMONIC CONVERSION EFFICIENCY

As second-harmonic generation is a quadratic process at low powers, the conversion efficiency per watt ($P_{\mathrm{SHG}}/P_{\mathrm{in}}^2$) remains constant (see Supporting Information). By measuring the second-harmonic power versus input power for a particular structure, we obtain a plot as shown in Figure 1d. Fitting this plot, we obtain a constant value for $P_{\mathrm{SHG}}/P_{\mathrm{in}}^2$. We measured 12 cavities (including different in-plane rotations) in each wafer orientation [$a = 580$ nm in the (001)-oriented wafer, $a = 620$ nm in the (111)B-oriented wafer], as discussed in the Far-Field Measurements section. The maximum measured conversion efficiency per watt for both (001)- and (111)B-oriented GaAs was 1.2%/W, although there was again a large structure-to-structure variation even at a particular in-plane rotation, perhaps due to the strong sensitivity to in- and out-coupling (see Supporting Information), which will vary due to small variations in structures as well as alignment. By comparison, previous studies in similar structures in GaP[17] reported a similar total conversion efficiency per watt of around 0.9%/W at telecommunications wavelengths and a much reduced efficiency per watt of 0.002%/W in GaAs at telecommunications wavelengths.[8] We discuss how this compares to simulations in the Simulations section.

Due to the symmetry of the nonlinear susceptibility tensor, the efficiency of the second-harmonic process will vary with in-plane rotation of the photonic crystal cavity (see Supporting Information). To verify the rotation dependence for structures in the (111)B orientation, we fabricated a second chip with more cavities with in-plane rotations relative to the $[2\bar{1}\bar{1}]$ direction. Rotations were every 15° from 0° to 180°, as shown in the SEM in Figure 4a, and the lattice constant was 620 nm. The cavities had a mean fundamental resonant wavelength of 1803.3 nm, with a standard deviation of 1.7 nm. The stripes visible in the SEM are an artifact of the SEM. We plot normalized efficiency per unit power versus rotation for two rows of structures with the same parameters, shown in red and blue in Figure 4b. The plots were normalized to the maximum value for each row, and the mean of the two is plotted in black, where we see a $\pi/3$ periodicity as a function of in-plane rotation. This is expected due to to the fact that a $\pi/3$ rotation in the (111) orientation is equivalent to an inversion of the crystal axes, combined with the π symmetry of the photonic crystal cavity (see Supporting Information). References 16 and 17 have previously reported variation in second-harmonic signal in (001)-oriented III–V semiconductors depending on the in-plane rotation of the structure.

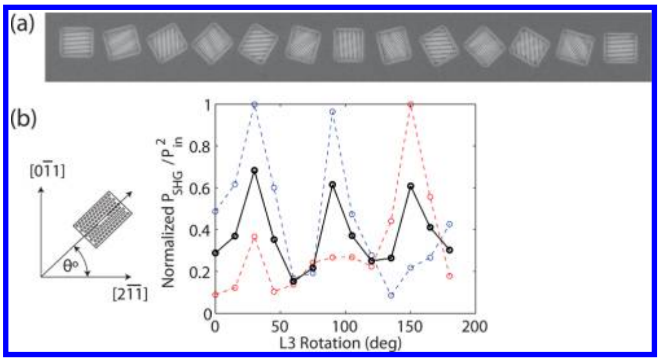

Figure 4. (a) SEM of a single row of structures fabricated in (111)B GaAs, with rotations every 15 degrees. (b) Red and blue lines show normalized efficiency per unit power for two different rows as shown in (a), with resonant wavelength at 1800 nm. Black line is the mean of the red and blue lines.

■ SIMULATIONS

We next perform simulations in order to try to reproduce the far-field *k*-space observed in experiment and the efficiency of the second-harmonic process. This is done by first simulating the fundamental mode and then using this to generate a spatial polarization with which we can simulate the second-harmonic mode. From these simulations we can estimate the in- and out-coupling efficiencies we should obtain using an objective lens with a numerical aperture of 0.95. Once we have the spatial profiles, coupling efficiencies, and Q factors of both modes, we can estimate the low power efficiency of the device. We additionally explore the parameter space around our device in order to determine the sensitivity of the device to design parameters and to explore the possibility to engineer higher efficiency devices.

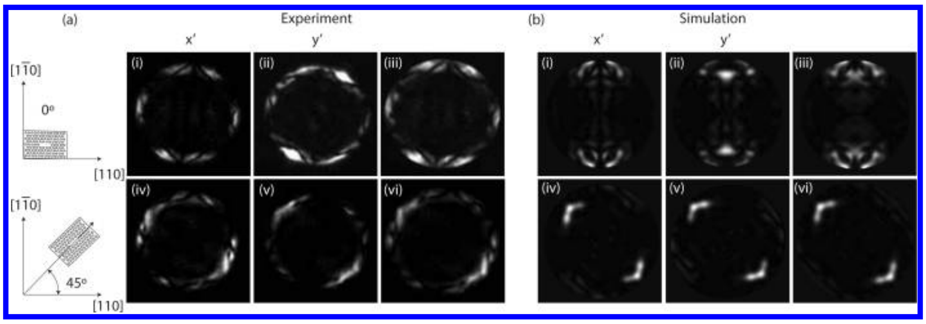

Figure 5. (a) Experimentally measured far-field of generated second harmonic on (001) GaAs wafer, as a function of L3 photonic crystal cavity in-plane rotation. The top/bottom row corresponds to the L3 cavity at 0/45° relative to the cleave ([110] or equivalent) axes. (i) and (iv) show the far-field for just the x polarization, while (ii) and (v) show the far-field for just the y polarization, and (iii) and (vi) show the total image. (b) Simulated far-fields for the parameters used in the experiment.

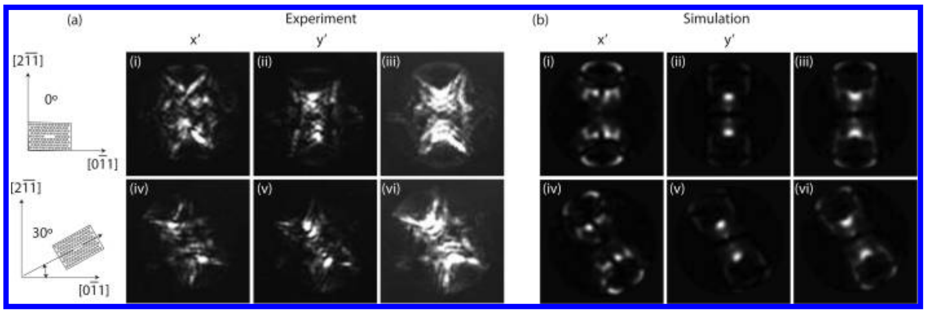

Figure 6. (a) Experimentally measured far-field of the generated second harmonic on the (111) GaAs wafer, as a function of L3 photonic crystal cavity in-plane rotation. The top/bottom row corresponds to the L3 cavity at 0/30° relative to the cleave ($[11\bar{2}]$ or equivalent) axes. (i) and (iv) show the far-field for just the x polarization, while (ii) and (v) show the far-field for just the y polarization, and (iii) and (vi) show the total image. (b) Simulated far-fields for the parameters used in the experiment.

The fundamental mode was simulated by finite difference time domain simulations (FDTD). As discussed in the Far-Field Measurements section, despite the fact that we use nominally the same membrane thickness, to maintain the same resonant wavelength we need to increase the lattice constant by 40 nm in (111)B GaAs compared to (001) GaAs. In order to precisely match the fundamental mode wavelengths to the simulation, the radius of the hole radii and thickness of the membrane were adjusted around the designed values. Simulations of the fundamental mode indicate that for a membrane thickness of 165 nm a radius of $0.28a$ is consistent with the measured resonant frequencies for (001)-oriented GaAs structures, while a radius of $0.3a$ is consistent with the (111)B-oriented GaAs resonant frequencies. The relative size of perturbed holes was maintained constant. However, we found better agreement with second-harmonic simulations by varying the membrane thickness.

The radiative (Q_{rad}) and total (Q_{tot}) Q factors of the photonic crystal cavities were calculated from simulations, in order to obtain an estimate for the cavity coupling efficiency. We take the coupling efficiency $\eta_1 = fQ_{\mathrm{tot}}/2Q_{\mathrm{rad}}$, where f is the fraction of the radiated light (coupled to the cavity from vertically above it) through the NA of the objective lens. This fraction is calculated from the fraction of the radiation vectors within the light cone that also have k-vectors within the NA of the lens. We simulate the far-field by performing the Fourier transform of the complex fields a distance s above the surface of the slab as described in refs 29 and 30.

In order to simulate the second-harmonic mode, we generate a polarization from the fundamental mode, which is the initial excitation for our simulation:

$$P_i = \epsilon_{\mathrm{bin}}\chi^{(2)}_{ijk}E_jE_k \quad i = x, y, z \tag{1}$$

where ϵ_{bin} is 1 wherever there is semiconductor and 0 in air. This generated polarization will be different in the case of the (001) and (111) orientations and will also depend on the rotation of the L3 cavity with respect to the crystal axes in the plane of the wafer (see Supporting Information). We calculate the far-field for the simulated modes to compare these to experiment. These modes were particularly sensitive to the membrane thickness of the structure. Therefore, we varied the membrane thickness of the cavity around the experimental values while maintaining the correct fundamental wavelength. For each simulation, we calculated the overlap of simulated and experimental k-space in order to find the best match (see Supporting Information).

Implicit so far has been the assumption that the nonlinearity is due to bulk effects, while the nanocavity employed has a significant surface to volume ratio. The symmetry of the surface is different from the bulk $\chi^{(2)}$ effect,[31] although in the case of (001)-GaAs the (001) surface (which is the main surface seen by the mode) nonlinearity still prevents TE−TE mode coupling. Our simulations of surface versus bulk overlap indicate that while the surface may contribute slightly to the second-harmonic signal, the main contribution is from the bulk $\chi^{(2)}$ nonlinearity. This is in agreement with the conclusions found in previous studies of photonic crystal cavities.[32] Experimentally, by performing measurements on a number of structures rotated in-plane, it should be possible to distinguish the surface from bulk contributions.[31] However, this effect is complicated due to the fact that the second-harmonic mode is very sensitive and will change depending on the excitation, and any measurement would need to be statistical over many

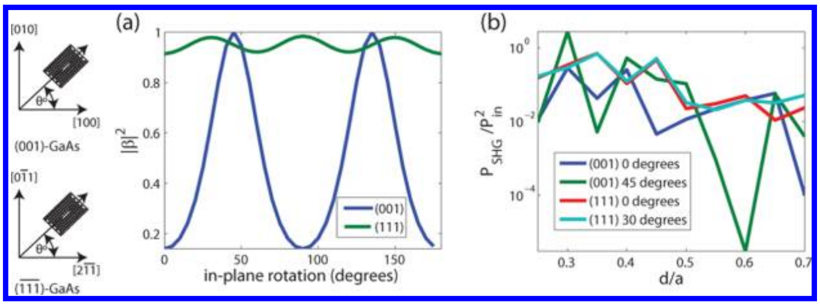

Figure 7. (a) Normalized simulated nonlinear overlap between fundamental and SHG modes versus in-plane rotation for (111) and (001) wafer orientations relative to the $[2\bar{1}\bar{1}]$ and [100] directions, respectively. (b) Simulated efficiency per unit power (W^{-1}) versus membrane thickness for a particular L3 cavity design and for (111) and (001) wafer orientations with different in-plane cavity rotations relative to the cleave axis.

structures, as the polarization is set by the in-plane rotation of the cavity. As there is significant structure-to-structure variation due to fabrication imperfections, such an effect may be impossible to measure. Even the rotation dependence of the surface will depend significantly on the presence of any native oxides or surface contamination.[33]

Figures 5 and 6 show (a) experimental and (b) simulated *k*-space images for (001) and (111) orientations, with simulations plotting up to NA = 0.95. For the (001) orientation, we compare the experimentally measured and simulated *k*-space images for both 0 and 45 deg rotations for the cavity mode with resonant frequency at 1800 nm, while for (111) orientation we compare 0 and 30 deg rotations with simulations. The (001)-oriented cavity simulation was consistent with a membrane thickness of 165 nm. The (111) orientation simulation indicated a membrane thickness of 150 nm.

For triply resonant cavity processes at low input powers, the second-harmonic power P_{SHG} is proportional to the input power P_{in} as

$$P_{SHG} = \frac{32\eta_1^2\eta_2 Q_1^2 Q_2|\beta_1|^2}{\omega_1}P_{in}^2 \tag{2}$$

(see Supporting Information), where Q_1 and Q_2 are the quality factors of the fundamental and second-harmonic modes, η_1 and η_2 are the input/output coupling efficiencies of the fundamental and second-harmonic modes, and $|\beta|^2$ is a nonlinear overlap integral given by[2,34]

$$\beta_1 = \frac{1}{4}\frac{\iiint d^3x\epsilon_0 \sum_{ijk}\chi_{ijk}^{(2)}E_{1i}^*(E_{1j}^*E_{2k} + E_{1k}^*E_{2j})}{\iiint d^3x\epsilon|E_1|^2\sqrt{\iiint d^3x\epsilon|E_2|^2}} \tag{3}$$

whose value for a particular set of modes depends on the magnitude and symmetry of $\chi^{(2)}$. From eq 2 we can see that the conversion efficiency is very sensitive to the Q factors of both modes, as well as to the coupling efficiency.

Using these simulations, we can make estimates of this nonlinear overlap integral, as well as of the total Q and coupling Q factors of the second-harmonic mode. We verify that the simulations give us the expected in-plane rotation dependence in Figure 7a, where we plot the nonlinear overlap $|\beta|^2$ (each normalized to its maximum value) versus the in-plane rotation for (001) and (111) orientations, and obtained the expected 60 and 90 deg symmetries. From eq 2, we can calculate the simulated efficiency per watt input power.

The fundamental and second-harmonic modes were simulated for increasing d/a (in an experiment corresponding to an increase in membrane thickness, with resonant wavelength maintained constant). The plot of P_{SHG}/P_{in}^2, shown in Figure 7b, shows that the geometry of the second-harmonic mode is very important in calculating the overall efficiencies. From this plot, we estimate efficiencies on the order of 10%/W for both (001) and (111) orientations, compared to the experimentally measured values on the order of 1%/W. The internal conversion efficiency can also be estimated using the simulated coupling efficiency values (around 30%) to give a simulated internal efficiency of 370%/W. These calculated coupling efficiencies are likely higher than the experimentally achieved coupling efficiency and could explain the discrepancy between simulated and measured values.

From this plot, we see that the particular second-harmonic mode excited is very important in determining the efficiency of the device. For example, depending on the particular second-harmonic mode, either the 0° or 45° in-plane rotation in the (001) orientation can have higher efficiency. The (111) and (001) orientations also vary in relative efficiencies depending on parameters, and therefore with knowledge of the second-harmonic mode we can use the wafer orientation in order to engineer higher efficiency devices. Having good control over these modes would also allow us to use microcavities in order to measure nonlinear properties of new materials, without needing to develop phase-matching and quasi-phase-matching techniques. However, this is challenging in these geometries, as the particular mode is very sensitive to the parameters of the device.

ENGINEERING HIGHER EFFICIENCY DEVICES

The experimentally achieved efficiency of second-harmonic generation in photonic crystal cavities has been limited by the difficulty of engineering multiple high-quality factor modes with a high degree of overlap.[16−18] This difficulty arises because the band gap of photonic crystals does not span a sufficiently large frequency range for $\chi^{(2)}$ processes, and there are no significant higher order band gaps. This means that only one of the modes of the photonic crystal cavity in the process is well-defined and has high Q. As discussed in this work and others,[11,16−18] the second-harmonic couples to leaky air band modes perturbed by the presence of the cavity, which have low Q factors and low overlap with the fundamental mode and are difficult to couple to for processes such as difference frequency conversion and optical parametric oscillation. The SHG process goes as the square of the fundamental; so as shown in eq 2, it is important that the fundamental mode have a large Q. However, since we are coupling at normal incidence, increasing the Q factor will in general lead to a decrease in the coupling efficiency, and therefore increasing the Q significantly beyond a few thousand does not lead to further improvement. Creating a well-defined coupling channel, such as a waveguide coupled to the photonic crystal cavity, would allow us to obtain increased benefit from higher Q. For the current structure, a better understanding of these modes outside the band gap in photonic crystals may help to engineer higher efficiency frequency conversion. The additional degree of freedom of choosing the symmetry of the effective $\chi^{(2)}$ is also beneficial in the design of resonators. Where individual resonators with high overlap and Q factors may not be sufficient, the ability to engineer doubly resonant microcavities opens up the possibility for generating highly nonlinear materials that phase-match via engineered dispersion[35] or quasi-phase-match[36] using coupled resonator arrays. There have been several proposals for designing photonic crystal cavities with multiple high-Q resonances and large frequency separations;[34,37−41] such a cavity could improve the efficiency of the process by several orders of magnitude.

Integration of nonlinear microcavities with quantum dots for quantum optics and quantum information processing is also of current interest. Cavities such as those used in this work could be useful for high signal-to-noise resonant excitation of InAs QDs.[10] Additionally, frequency conversion of flying qubits to telecommunications wavelength or to optimal detection wavelengths is desirable[42] and has been demonstrated using off-chip periodically poled lithium niobate waveguides. Self-frequency conversion of high-density quantum dots in a photonic crystal cavity has been recently demonstrated,[12,24] but frequency conversion of single quantum dots coupled to on-chip microcavities has yet to be demonstrated. In particular, frequency conversion between InAs QD wavelengths and telecommunications wavelength requires intracavity difference frequency generation, which is again challenging, due to the long wavelength of the pump and difficulties in engineering photonic crystal cavities with well-defined and overlapping modes at sufficiently large wavelength separations. This work demonstrates the characterization and operation of these cavities in GaAs at longer wavelengths than previously demonstrated.

Creating a highly nonlinear element such as a photonic crystal in a $\chi^{(2)}$ material is also of interest itself for quantum information processing,[43] for generation of single photons via photon blockade,[44] or for strongly coupling photons at two different wavelengths.[45]

CONCLUSION

We demonstrate second-harmonic generation below the band gap in photonic crystal cavities in (001)- and (111)B-oriented GaAs. We fabricate photonic crystal structures in both (111)B- and (001)-oriented GaAs at different orientations with respect to the crystal axes of the GaAs substrate and match the rotation dependence and far-field patterns to simulation. We discuss how these results are relevant to engineering higher efficiency on-chip nonlinear frequency conversion in photonic crystal cavities.

ASSOCIATED CONTENT

Ⓢ Supporting Information

Details of the simulation and analysis procedures. This material is available free of charge via the Internet at http://pubs.acs.org.

AUTHOR INFORMATION

Corresponding Author

*E-mail: bucklesm@stanford.edu.

Notes

The authors declare no competing financial interest.

ACKNOWLEDGMENTS

Financial support was provided by the Air Force Office of Scientic Research, MURI Center for Multifunctional Light-matter Interfaces Based on Atoms and Solids, National Science Graduate Fellowships, and Stanford Graduate Fellowships. This work was performed in part at the Stanford Nanofabrication Facility of NNIN supported by the National Science Foundation under Grant No. ECS-9731293 and at the Stanford Nano Center. J.V. also thanks the Alexander von Humboldt Foundation for support. K.G.L. acknowledges support from the Swiss National Science Foundation.

REFERENCES

(1) Liscidini, M.; Andreani, L. C. Highly efficient second-harmonic generation in doubly resonant planar microcavities. *Appl. Phys. Lett.* **2004**, *85*, 1883−1885.

(2) Rodriguez, A.; Soljačić, M.; Joannopoulos, J. D.; Johnson, S. G. $\chi^{(2)}$ and $\chi^{(3)}$ harmonic generation at a critical power in inhomogeneous doubly resonant cavities. *Opt. Express* **2007**, *15*, 7303−7318.

(3) Fiore, A.; Berger, V.; Rosencher, E.; Bravetti, P.; Nagle, J. Phase matching using an isotropic nonlinear optical material. *Nature* **1998**, *391*, 463−466.

(4) Eyres, L. A.; Tourreau, P. J.; Pinguet, T. J.; Ebert, C. B.; Harris, J. S.; Fejer, M. M.; Becouarn, L.; Gerard, B.; Lallier, E. All-epitaxial fabrication of thick, orientation-patterned GaAs films for nonlinear optical frequency conversion. *Appl. Phys. Lett.* **2001**, *79*, 904−906.

(5) Kuo, P. S.; Bravo-Abad, J.; Solomon, G. S. Second-harmonic generation using quasi-phasematching in a GaAs whispering-gallery-mode microcavity. *Nat. Commun.* **2014**, *5*.

(6) Stievater, T. H.; Mahon, R.; Park, D.; Rabinovich, W. S.; Pruessner, M. W.; Khurgin, J. B.; Richardson, C. J. K. Mid-infrared difference-frequency generation in suspended GaAs waveguides. *Opt. Lett.* **2014**, *39*, 945−948.

(7) Vakhshoori, D.; Fischer, R.; Hong, M.; Sivco, D.; Zydzik, G.; Chu, G.; Cho, A. Blue-green surface-emitting second-harmonic generators on (111)B GaAs. *Appl. Phys. Lett.* **1991**, *59*, 896.

(8) Buckley, S.; Radulaski, M.; Biermann, K.; Vučković, J. Second harmonic generation in photonic crystal cavities in (111)-oriented GaAs. *Appl. Phys. Lett.* **2013**, *103*, 211117.

(9) Khankhoje, U. K.; Kim, S.-H.; Richards, B. C.; Hendrickson, J.; Sweet, J.; Olitzky, J. D.; Khitrova, G.; Gibbs, H. M.; Scherer, A. Modelling and fabrication of GaAs photonic-crystal cavities for cavity quantum electrodynamics. *Nanotechnology* **2010**, *21*, 065202.

(10) Rivoire, K.; Buckley, S.; Majumdar, A.; Kim, H.; Petroff, P.; Vučković, J. Fast quantum dot single photon source triggered at telecommunications wavelength. *Appl. Phys. Lett.* **2011**, *98*, 083105−083105−3.

(11) Buckley, S.; Rivoire, K.; Hatami, F.; Vučković, J. Quasiresonant excitation of InP/InGaP quantum dots using second harmonic generated in a photonic crystal cavity. *Appl. Phys. Lett.* **2012**, *101*, 161116−161116−4.

(12) Ota, Y.; Watanabe, K.; Iwamoto, S.; Arakawa, Y. Nanocavity-based self-frequency conversion laser. *Opt. Express* **2013**, *21*, 19778−19789.

(13) Xiong, C.; Pernice, W.; Ryu, K. K.; Schuck, C.; Fong, K. Y.; Palacios, T.; Tang, H. X. Integrated GaN photonic circuits on silicon (100) for second harmonic generation. *Opt. Express* **2011**, *19*, 10462−10470.

(14) Levy, J. S.; Foster, M. A.; Gaeta, A. L.; Lipson, M. Harmonic generation in silicon nitride ring resonators. *Opt. Express* **2011**, *19*, 11415−11421.

(15) Pernice, W. H. P.; Xiong, C.; Schuck, C.; Tang, H. X. Second harmonic generation in phase matched aluminum nitride waveguides

and micro-ring resonators. *Appl. Phys. Lett.* **2012**, *100*, 223501−223501−4.

(16) McCutcheon, M. W.; Young, J. F.; Rieger, G. W.; Dalacu, D.; Frédérick, S.; Poole, P. J.; Williams, R. L. Experimental demonstration of second-order processes in photonic crystal microcavities at submilliwatt excitation powers. *Phys. Rev. B: Condens. Matter Mater. Phys.* **2007**, *76*, 245104.

(17) Rivoire, K.; Lin, Z.; Hatami, F.; Masselink, W. T.; Vučković, J. Second harmonic generation in gallium phosphide photonic crystal nanocavities with ultralow continuous wave pump power. *Opt. Express* **2009**, *17*, 22609−22615.

(18) Diziain, S.; Geiss, R.; Zilk, M.; Schrempel, F.; Kley, E.-B.; Tünnermann, A.; Pertsch, T. Second harmonic generation in free-standing lithium niobate photonic crystal L3 cavity. *Appl. Phys. Lett.* **2013**, *103*, 051117−051117−4.

(19) Ilchenko, V. S.; Matsko, A. B.; Savchenkov, A. A.; Maleki, L. Low-threshold parametric nonlinear optics with quasi-phase-matched whispering-gallery modes. *J. Opt. Soc. Am. B* **2003**, *20*, 1304−1308.

(20) Fürst, J. U.; Strekalov, D. V.; Elser, D.; Lassen, M.; Andersen, U. L.; Marquardt, C.; Leuchs, G. Naturally Phase-Matched Second-Harmonic Generation in a Whispering-Gallery-Mode Resonator. *Phys. Rev. Lett.* **2010**, *104*, 153901.

(21) Förtsch, M.; Fürst, J. U.; Wittmann, C.; Strekalov, D.; Aiello, A.; Chekhova, M. V.; Silberhorn, C.; Leuchs, G.; Marquardt, C. A versatile source of single photons for quantum information processing. *Nat. Commun.* **2013**, *4*, 1818.

(22) Joannopoulos, J. D.; Johnson, S. G.; Winn, J. N.; Meade, R. D. *Photonic Crystals: Molding the Flow of Light*, 2nd ed.; Princeton University Press, 2011.

(23) Shoji, I.; Kondo, T.; Kitamoto, A.; Shirane, M.; Ito, R. Absolute scale of second-order nonlinear-optical coefficients. *J. Opt. Soc. Am. B* **1997**, *14*, 2268−2294.

(24) Ota, Y.; Watanabe, K.; Iwamoto, S.; Arakawa, Y. Self-frequency summing in quantum dot photonic crystal nanocavity lasers. *Appl. Phys. Lett.* **2013**, *103*, 243115.

(25) Palik, E. D. *Handbook of Optical Constants of Solids, Vol.s I, II, and III: Subject Index and Contributor Index*; Elsevier Science & Tech, 1985.

(26) Toishi, M.; Englund, D.; Faraon, A.; Vučković, J. High-brightness single photon source from a quantum dot in a directional-emission nanocavity. *Opt. Express* **2009**, *17*, 14618−14626.

(27) Portalupi, S. L.; Galli, M.; Reardon, C.; Krauss, T.; O'Faolain, L.; Andreani, L. C.; Gerace, D. Planar photonic crystal cavities with far-field optimization for high coupling efficiency and quality factor. *Opt. Express* **2010**, *18*, 16064−16073.

(28) Altug, H.; Vuckovic, J. Photonic crystal nanocavity array laser. *Opt. Express* **2005**, *13*, 8819.

(29) Vuckovic, J.; Loncar, M.; Mabuchi, H.; Scherer, A. Optimization of the Q factor in photonic crystal microcavities. *IEEE J. Quantum Electron.* **2002**, *38*, 850−856.

(30) Taflove, A.; Hagness, S. C. *Computational electrodynamics: the finite-difference time-domain method*; Artech House: Boston, 2005.

(31) Stehlin, T.; Feller, M.; Guyot-Sionnest, P.; Shen, Y. R. Optical second-harmonic generation as a surface probe for noncentrosymmetric media. *Opt. Lett.* **1988**, *13*, 389−391.

(32) McCutcheon, M. W.; Rieger, G. W.; Cheung, I. W.; Young, J. F.; Dalacu, D.; Frdrick, S.; Poole, P. J.; Aers, G. C.; Williams, R. L. Resonant scattering and second-harmonic spectroscopy of planar photonic crystal microcavities. *Appl. Phys. Lett.* **2005**, *87*, 221110.

(33) Armstrong, S. R.; Hoare, R. D.; Pemble, M. E.; Povey, I. M.; Stafford, A.; Taylor, A. G. Optical second harmonic generation studies of the nature of the GaAs(100) surface in air. *J. Cryst. Growth* **1992**, *120*, 94−97.

(34) Burgess, I. B.; Zhang, Y.; McCutcheon, M. W.; Rodriguez, A. W.; Bravo-Abad, J.; Johnson, S. G.; Loncar, M. Design of an efficient terahertz sourceusing triply resonant nonlinearphotonic crystal cavities. *Opt. Express* **2009**, *17*, 20099−20108.

(35) Xu, Y.; Lee, R. K.; Yariv, A. Propagation and second-harmonic generation of electromagnetic waves in a coupled-resonator optical waveguide. *J. Opt. Soc. Am. B* **2000**, *17*, 387−400.

(36) Dumeige, Y. Quasi-phase-matching and second-harmonic generation enhancement in a semiconductor microresonator array using slow-light effects. *Phys. Rev. A: At., Mol., Opt. Phys.* **2011**, *83*, 045802.

(37) Zhang, Y.; McCutcheon, M. W.; Burgess, I. B.; Lončar, M. Ultra-high-Q TE/TM dual-polarized photonic crystal nanocavities. *Opt. Lett.* **2009**, *34*, 2694−2696.

(38) Thon, S. M.; Irvine, W. T. M.; Kleckner, D.; Bouwmeester, D. Polychromatic photonic quasicrystal cavities. *Phys. Rev. Lett.* **2010**, *104*, 243901.

(39) McCutcheon, M. W.; Chang, D. E.; Zhang, Y.; Lukin, M. D.; Lončar, M. Broadband frequency conversion and shaping of single photons emitted from a nonlinear cavity. *Opt. Express* **2009**, *17*, 22689−22703.

(40) Rivoire, K.; Buckley, S.; Vučkovi, J. Multiply resonant photonic crystal nanocavities for nonlinear frequency conversion. *Opt. Express* **2011**, *19*, 22198−22207.

(41) Rivoire, K.; Buckley, S.; Vučković, J. Multiply resonant high quality photonic crystal nanocavities. *Appl. Phys. Lett.* **2011**, *99*, 013114−013114−3.

(42) Buckley, S.; Rivoire, K.; Vučković, J. Engineered quantum dot single-photon sources. *Rep. Prog. Phys.* **2012**, *75*, 126503.

(43) Mabuchi, H. Qubit limit of cavity nonlinear optics. *Phys. Rev. A: At., Mol., Opt. Phys.* **2012**, *85*, 015806.

(44) Majumdar, A.; Gerace, D. Single-photon blockade in doubly resonant nanocavities with second-order nonlinearity. *Phys. Rev. B: Condens. Matter Mater. Phys.* **2013**, *87*, 235319.

(45) Irvine, W. T. M.; Hennessy, K.; Bouwmeester, D. Strong coupling between single photons in semiconductor microcavities. *Phys. Rev. Lett.* **2006**, *96*, 057405.